Symmetry-Based Phenomenological Model for Magnon Transport in a Multiferroic

Isaac A. Harris,[1,*] Sajid Husain,[2,3,*,†] Peter Meisenheimer,[3] Maya Ramesh,[4] Hyeon Woo Park,[5] Lucas Caretta,[6] Darrell G. Schlom,[4,7,8] Zhi Yao,[9] Lane W. Martin,[3,10–13] Jorge Íñiguez-González,[14,15] Se Kwon Kim,[5] and Ramamoorthy Ramesh[1,3,2,11,10,13,‡]

[1]*Department of Physics, University of California, Berkeley, California, USA*
[2]*Materials Science Division, Lawrence Berkeley National Laboratory, Berkeley, California, USA*
[3]*Department of Materials Science and Engineering, University of California, Berkeley, California, USA*
[4]*Department of Materials Science and Engineering, Cornell University, Ithaca, New York, USA*
[5]*Department of Physics, Korea Advanced Institute of Science and Technology, Daejon, Korea*
[6]*School of Engineering, Brown University, Providence, Rhode Island, USA*
[7]*Kavli Institute at Cornell for Nanoscale Science, Ithaca, New York 14853, USA*
[8]*Leibniz-Institut für Kristallzüchtung, Max-Born-Straße 2, 12489 Berlin, Germany*
[9]*Applied Mathematics and Computational Research Division, Lawrence Berkeley National Laboratory, Berkeley, California 94720, USA*
[10]*Department of Materials Science and NanoEngineering, Rice University, Houston, Texas, USA*
[11]*Department of Physics and Astronomy, Rice University, Houston, Texas, USA*
[12]*Department of Chemistry, Rice University, Houston, Texas, USA*
[13]*Rice Advanced Materials Institute, Rice University, Houston, Texas, USA*
[14]*Materials Research and Technology Department, Luxembourg Institute of Science and Technology, Esch-sur-Alzette, Luxembourg*
[15]*Department of Physics and Materials Science, University of Luxembourg, Belvaux, Luxembourg*

(Received 11 April 2024; accepted 12 November 2024; published 2 January 2025)

Magnons—carriers of spin information—can be controlled by electric fields in the multiferroic $BiFeO_3$ (BFO), a milestone that brings magnons closer to application in future devices. The origin of magnon-spin currents in BFO, however, is not fully understood due to BFO's complicated magnetic texture. In this Letter, we present a phenomenological model to elucidate the existence of magnon spin currents in generalized multiferroics by examining the symmetries inherent to their magnetic and polar structures. This model is grounded in experimental data obtained from BFO and its derivatives, which informs the symmetry operations and resultant magnon behavior. By doing so, we address the issue of symmetry-allowed, switchable magnon spin transport in multiferroics, thereby establishing a critical framework for comprehending magnon transport within complex magnetic textures.

DOI: 10.1103/PhysRevLett.134.016703

Magnons, quanta of spin waves, have become the ideal carriers of information in future spin-based technologies [1–4]. Magnons can carry information through insulating antiferromagnets, which are desirable candidate materials for novel magnetic storage technologies [5–7]. While manipulating the magnetic order parameter of most antiferromagnets is impractical in device applications, the antiferromagnetic order of multiferroic bismuth ferrite, $BiFeO_3$ (BFO), is switchable by an electric field due to the magnetoelectric coupling between ferroelectricity and antiferromagnetism [8–13]. Electric field control of magnon transport through BFO has been recently demonstrated [12,14–18]; however, the microscopic mechanism of the magnon-mediated spin transport remains unknown. This is in contrast to ferro(ferri)magnets, where the spin carried by magnons is simply controlled by the magnetic field, and the microscopic origins of spin transport are well described [19–21].

Despite the complexity of the magnetic structure in BFO [22,23], a simple phenomenological approach to magnon-mediated spin transport in a generalized magnetic texture would offer insight into the physical mechanisms of electric-field-controlled magnon transport. By applying mirror and time-reversal operations on the magnon propagation, it is possible to predict the behavior of the spin current based on the transformations of the magnetic texture under these operations. We apply this to thermally excited magnon-spin transport in three model BFO samples with different spin-cycloid configurations, where the behavior of the polarization and the magnetic texture under different electric fields has been mapped. We find that the model's predictions, based on the symmetries associated with the samples' magnetic textures, match

*These authors contributed equally to this work.
†Contact author: shusain@berkeley.gov
‡Contact author: rramesh@berkeley.edu

the measured magnon-transport data. These results show that this model can be a powerful tool to guide further studies into the microscopic origin of magnon-mediated spin transport, as well as predict the qualities of magnon transport in new multiferroic systems.

Thin films of BFO and its derivative $Bi_{0.85}La_{0.15}FeO_3$ (BLFO) were deposited using pulsed-laser deposition and molecular-beam epitaxy (Supplemental Material note 1 [24]), and platinum (Pt) was sputtered for voltage detection of spin currents arising from nonlocal magnon excitations [21,29,30] [Fig. 1(a)]. An electric field is applied between the two wires to set the polarization state of the BFO (BLFO) while disconnecting the source current and voltage detector. Then, the electric field is turned off and the current source is activated across one wire, while the lock-in voltage detector is across the other. Here, voltage measurements reference the second harmonic of the low frequency (7 Hz) source current [21,29] to select magnons generated from the spin-Seebeck effect (SSE). This is repeated (automatically through a Keithley switchbox) over a range of electric fields to extract the inverse spin-Hall effect (ISHE) voltage (V_{ISHE}) as a function of electric field, and then the identities of the source and detector wires are switched to extract the data from a thermal gradient applied in the opposite direction (Fig. 3 and Supplemental Material note 2 [24]).

To tie the observed magnon signal to the microscopic magnetic structure, we begin with a phenomenological model for magnon transport in a generic multiferroic. By extending the formalism from prior thermal magnon works [20,31,32], we write the spin-current density $\mathbf{j}_s(\mathbf{r})$ (traveling in the z direction) from magnon modes indexed by μ:

$$\mathbf{j}_s(\mathbf{r}) \approx \sum_{\mu} \langle \mathbf{S} \rangle_{\mu} \int d^3k\, v_{\mu k,z}(n_{\mu k} - n^0_{\mu k}). \tag{1}$$

The vector part of $\mathbf{j}_s(\mathbf{r})$ denotes the spin polarization direction, $\langle \mathbf{S} \rangle_{\mu}$ is the expected value of spin carried by magnon mode μ [33], $v_{\mu k,z}$ is the z component of the group velocity $\mathbf{v}_{\mu k} = \hat{\mathbf{k}}(\partial \omega_k / \partial k)$, $n_{\mu k}(\mathbf{r})$ is the total number of magnons, and $n_{\mu k} - n^0_{\mu k}$ is the number of magnons in excess of equilibrium at any given location $\mathbf{r}$, in mode μ with wave vector k. Further details can be found in Supplemental Material note 3 [24]. These nonequilibrium magnons, represented pictorially [Fig. 1(a)], are responsible for the finite spin-current output. This spin-current density is integrated over the detector surface S to get the total spin current $\mathbf{I}_s$ entering the detector wire:

$$\mathbf{I}_s = \int_S d^2r\, \mathbf{j}_s(\mathbf{r}) \approx \sum_{\mu} \langle \mathbf{S} \rangle_{\mu} \eta_{\mu} \tag{2}$$

where

$$\eta_{\mu} = \int_S d^2r d^3k\, v_{\mu k,z}(n_{\mu k} - n^0_{\mu k}). \tag{3}$$

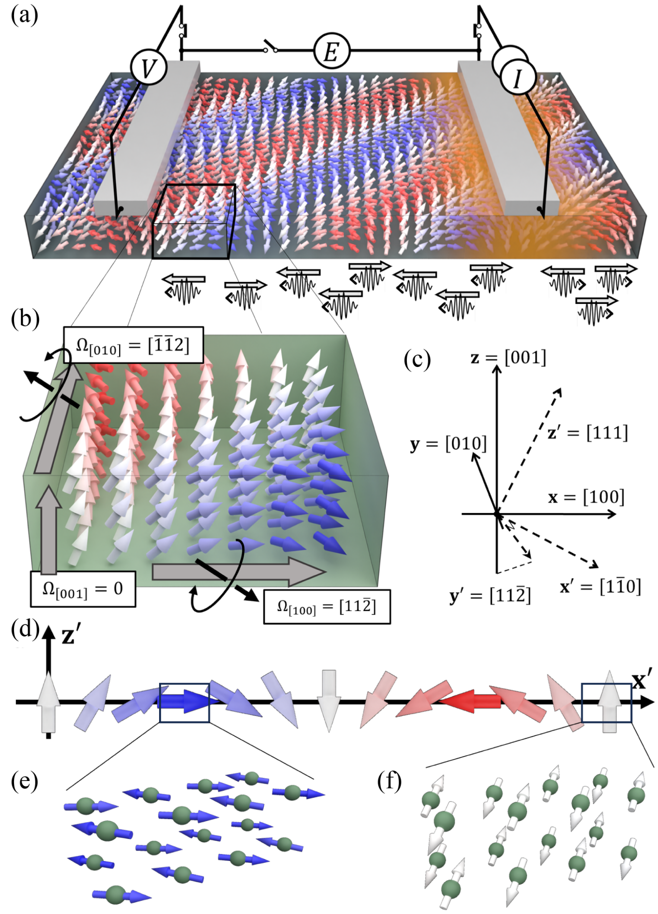

FIG. 1. (a) Magnons (represented by wavepackets here) with $\langle S_x \rangle \sim \pm\hat{\mathbf{x}}$, as notated by the block gray arrows, diffuse along the temperature gradient through the BFO/BLFO and impart their spin to the detector, generating an ISHE voltage. (b) The colored arrows represent the local Néel vector in the BFO. The polarization is along $\mathbf{z}' = [111]$ and the cycloid propagation direction is $\mathbf{x}' = [1\bar{1}0]$. The red and blue coloring gives the net moment due to canting, as would be detected in nitrogen vacancy (NV) microscopy. The vector $\mathbf{\Omega_b}$ represents the axis around which the Néel vector rotates along the direction $\mathbf{b}$. Looking at the change of the Néel vector along the $\mathbf{b} = [100]$, [010], or [001] directions, the Néel vector rotates clockwise, counterclockwise, or not at all around $[\bar{1}\,\bar{1}\,2]$, so $\mathbf{\Omega}_{[100],[010],[001]} = [11\bar{2}], [\bar{1}\,\bar{1}\,2], 0$. (c) The device axes has $\mathbf{x}$ parallel to the applied field and temperature gradient, $\mathbf{y}$ parallel to the Pt wires, and $\mathbf{z}$ as the film normal. Cycloid (primed) coordinates have $\mathbf{z}'$ parallel to the BFO polarization, $\mathbf{x}'$ parallel to the cycloid propagation axis, and $\mathbf{y}' = \mathbf{z}' \times \mathbf{x}'$ normal to the plane of the cycloid, which is shown in (d). (e),(f) The atom to atom variation in magnetic moment from the spin cycloid drawn to scale, including the spin density wave (not drawn to scale). We note that in (a),(b),(d) the arrows represent the average local Néel vector; however, in (e),(f) they represent the atomic magnetic dipoles.

Here, we have introduced η_{μ} as the extent to which the magnon mode μ contributes its spin $\langle \mathbf{S} \rangle_{\mu}$ to the detector wire. As a phenomenological function, η_{μ} is dependent on (a) the underlying effective Hamiltonian and the magnetic ground state Ψ, (b) the direction of the magnon diffusion $\hat{\mathbf{q}}$, and (c) the device geometry, which is effectively constant throughout all of the studies.

In a multiferroic, an electric field along $\hat{\mathbf{e}}$ can be used to switch between different ferroelectric (polarization) states, which correspond to different magnetic ground states $\Psi^{\hat{\mathbf{e}}}$. Furthermore, the direction of the thermal gradient (i.e., the direction of magnon diffusion $\hat{\mathbf{q}}$) can also be changed. In our experiment, we can alternate between $\hat{\mathbf{q}} = \pm\hat{\mathbf{x}}$ by switching the identity of the source wire and detector wire, thereby switching the direction of the temperature gradient. We switch the ferroelectric state by poling with positive or negative voltage across the detector and source wires, giving $\hat{\mathbf{e}} = \pm\hat{\mathbf{x}}$, where $\hat{\mathbf{e}}$ is the direction of the poling field above the critical field (Supplemental Material note 2 [24]). Thus, we write $\eta_\mu^{\hat{\mathbf{e}}}(\hat{\mathbf{q}})$ for the magnetic ground state $\Psi^{\hat{\mathbf{e}}}$ as a function of $\hat{\mathbf{q}}$. The nonlocal voltage, $V = R_{\mathrm{Pt}}\theta_{\mathrm{Pt}}(\mathbf{I}_s \cdot \hat{\mathbf{x}})$ is then also a function of $\Psi^{\hat{\mathbf{e}}}$ and $\hat{\mathbf{q}}$ ($\mathcal{I}$ row of Fig. 2). R_{Pt} and θ_{Pt} are the resistance and the spin-Hall angle of Pt. We are only interested in the $\mathbf{x}$ component of $\mathbf{I}_s$ because the ISHE current is a cross product between the spin-current direction, $\hat{\mathbf{z}}$, and the spin-current polarization, $\mathbf{I}_s$. While the magnitude of the nonlocal voltage V will also depend on the absolute temperature and the magnitude of the temperature gradient, these variables are fixed in our experiments in order to focus on the symmetry-based phenomenological model.

Next, we consider symmetry operations on the ground state, experimental configuration, and magnon dynamics to impose constraints on the four values $V_{\mathrm{ISHE}} \equiv V^{\hat{\mathbf{e}}}(\hat{\mathbf{q}})$ (Fig. 2) for $\hat{\mathbf{e}}, \hat{\mathbf{q}} = \pm\hat{\mathbf{x}}$. First, we consider the time reversal operation $\mathcal{T}$. A magnetic ground state with unpaired spins will break time-reversal symmetry; however, it is possible that the action of $\mathcal{T}$ on a magnetic texture is equivalent to a translation. For a translation in such a periodic magnetic texture with no global net magnetization, the magnon dynamics (i.e., diffusion, spin transport) integrated over an area much larger than the periodicity of the texture will be invariant under the translation, and thus will also be invariant under $\mathcal{T}$.

For any thermal magnon mode μ in such a magnetic texture, the action of $\mathcal{T}$ will transform the mode μ into mode μ', with spin and diffusion reversed, as shown schematically ($\mathcal{T}$ row of Fig. 2). Because of the invariance of the magnetic texture under $\mathcal{T}$, however, the dynamics encapsulated by η will be the same for both modes. Summing over all modes μ' to get a nonlocal voltage, we find that $V^{\hat{\mathbf{e}}}(-\hat{\mathbf{q}}) = -V^{\hat{\mathbf{e}}}(\hat{\mathbf{q}})$, which can be seen by combining the first two equations in the $\mathcal{T}$ row with the equation in the $\mathcal{I}$ row of Fig. 2. When the two-hysteresis measurements of V_{ISHE} are made for such a multiferroic texture and the four voltage measurements are extracted, the above condition causes the polarity of the hysteresis to reverse, and the ΔV_{ISHE} of the hysteresis to stay the same in switching from a $+\hat{\mathbf{q}}$ measurement to a $-\hat{\mathbf{q}}$ measurement as depicted in the $\mathcal{T}$ row of Fig. 2.

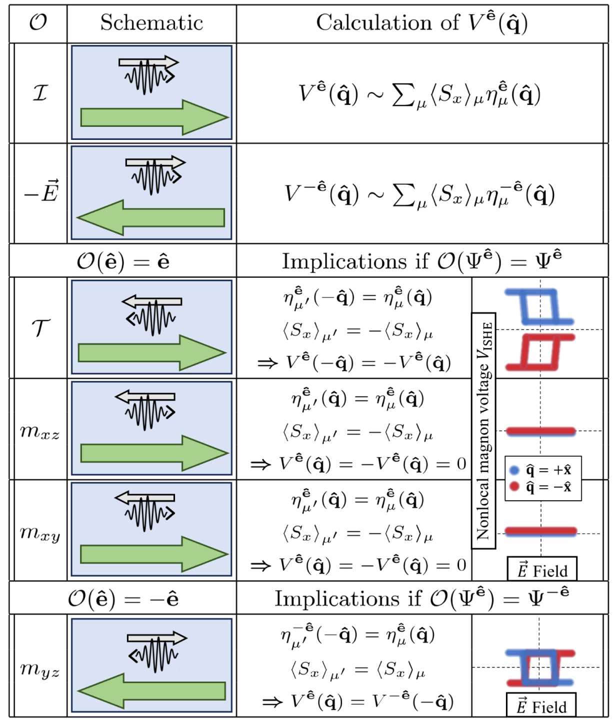

FIG. 2. Symmetry operations on a magnon mode μ with spin $\langle\mathbf{S}\rangle_\mu \| \hat{\mathbf{x}}$ diffusing in the $\hat{\mathbf{x}}$ direction, through a multiferroic poled along $\hat{\mathbf{x}}$. The black arrow attached to the wavepacket denotes the magnon diffusion direction, the gray arrow denotes the magnon spin direction, and the large green arrow denotes poling direction. The rows show, from top to bottom, the identity, electric field poling, time reversal, and mirror operations over the xz, xy, and yz planes. If the material (blue background) is invariant under the operations, we would expect each of the mathematical relations and their reflections on the measured magnon signal (as shown in the implications column) to hold true. We note that the $V^{\hat{\mathbf{e}}}(\hat{\mathbf{q}})$ values in the hypothetical magnon signals shown here are arbitrary.

Any symmetry operation $\mathcal{O}$ can be analyzed in this way to find implications in the magnetic texture on the V_{ISHE} measurements. This process is done for three mirror operations m_{xz}, m_{xy}, and m_{yz} (Fig. 2) over the xz, xy, and yz planes relative to the device geometry [see the unprimed coordinate system in Fig. 1(c)]. We note that upon applying m_{yz}, the poling direction is flipped, so the magnetic texture $m_{yz}(\Psi^{\hat{\mathbf{e}}})$ must be compared to the oppositely poled multiferroic texture $\Psi^{-\hat{\mathbf{e}}}$, as indicated by the table (Fig. 2). See Supplemental Material Fig. 4 [24] for visualization of these symmetry operations on the spin cycloid.

To test this model, we choose a set of three samples with different magnetic textures (Supplemental Material note 4 [24]). Sample I is a 50-nm-thick BFO film grown on a $TbScO_3$ (110) substrate, with wires patterned parallel to the 109° ferroelectric stripe domains [18]. Samples II and III are 45-nm-thick BLFO films grown on $DyScO_3$ (110) substrates, with wires patterned parallel to $[100]_{pc}$ and $[010]_{pc}$ (pc denotes pseudocubic), respectively [17]. All subsequent vectors are written in pseudocubic notation. Samples I and III have one variant of spin cycloid within the poled area, but sample II has two variants, with propagation vectors as noted (Fig. 3). The spin cycloid ground state of BFO, with average Néel vectors sketched in Fig. 1(d) and with Fe magnetic moments sketched in Figs. 1(e) and 1(f), is given by Fishman *et al.* [34]. Our first observation is that for all samples, $\mathcal{T}$, which flips each spin, is equivalent to a translation by half a period of the cycloid (Supplemental Material note 5 [24]). Since the magnetic texture is thus invariant under $\mathcal{T}$, we expect the V_{ISHE} data to exhibit the corresponding implications as shown (Fig. 2).

Measurements of V_{ISHE} for the three samples are provided (Fig. 3), and it can be seen that the polarity of the hysteresis is reversed while the magnitude of ΔV_{ISHE} remains the same upon switching $\hat{\mathbf{q}}$, as expected from the $\mathcal{T}$ invariance. While each sample has a 5–20 nV offset, we surmise that this could be from a gradient in the $\mathbf{z}$ direction and the resulting spin transport [35].

To analyze the mirror-symmetry operations, we take a closer look at the cycloidal texture in each domain. The precise determination of the polarization direction $\mathbf{z}'$ and the cycloid-propagation direction $\mathbf{x}'$ are discussed in Supplemental Material note 4 [24]. The rotation of the Néel vector around the cycloid plane normal $\mathbf{y}'$ [Fig. 1(c)] changes under the mirror operations (Fig. 3 and Supplemental Material Fig. 4 [24]).

Since $\mathbf{y}'$ depends on the choice of $\mathbf{x}'$, we define $\mathbf{\Omega_b}$ as the rotation of the Néel vector as measured along $\mathbf{b}$ [Fig. 1(b)]:

$$\mathbf{\Omega_b} = (\mathbf{b} \cdot \mathbf{x}')\mathbf{y}'. \tag{4}$$

It is clear that this observable does not depend on the sign of $\mathbf{x}'$ chosen. Figure 3 presents calculations for the three different BFO samples of $\mathbf{\Omega_b}$ with $\mathbf{b} = [100]$, [010], and [001], in the two different experimental configurations ($\hat{\mathbf{e}} = +\hat{\mathbf{x}}$, identity, or $\hat{\mathbf{e}} = -\hat{\mathbf{x}}$, $\vec{E}$ poled) and under the three different mirror operations (acting on $\Psi^{\hat{\mathbf{e}}}$ for $\hat{\mathbf{e}} = +\hat{\mathbf{x}}$). Although only the directions are recorded here, the results hold if the magnitudes are included. The corresponding V_{ISHE} data is included to the right for comparison. Sample I [Fig. 3(a)] has ~20-nm-wide stripy ferroelectric domains with polarizations $\mathbf{z}_1'$ and $\mathbf{z}_2'$ at a 109° angle that lead to a single variant spin cycloid with a propagation direction $\mathbf{x}'$ which is perpendicular to both $\mathbf{z}_1'$ and $\mathbf{z}_2'$ and a cycloidal plane given by $\hat{\mathbf{y}}' = \frac{1}{2}(\mathbf{z}_1' + \mathbf{z}_2') \times \hat{\mathbf{x}}'$ [18]. We find that under the action of any mirror symmetry, $\mathbf{\Omega_b}$ changes, and so we expect no further than the $\mathcal{T}$ implications in the signal. The data reflect that symmetry, and show only the signatures of $\mathcal{T}$ invariance.

(a) Sample I

Operation	$\mathbf{z}'$	$\mathbf{x}'$	$\mathbf{y}'$	$\mathbf{\Omega}_{[100]}$	$\mathbf{\Omega}_{[010]}$	$\mathbf{\Omega}_{[001]}$
Identity	$[111]$ $[1\bar{1}\bar{1}]$	$[01\bar{1}]$	$[011]$	0	$[011]$	$[0\bar{1}\bar{1}]$
m_{xz}	$[1\bar{1}1]$ $[11\bar{1}]$	$[0\bar{1}\bar{1}]$	$[01\bar{1}]$	0	$[0\bar{1}1]$	$[0\bar{1}1]$
m_{xy}	$[11\bar{1}]$ $[1\bar{1}1]$	$[011]$	$[0\bar{1}1]$	0	$[0\bar{1}1]$	$[0\bar{1}1]$
m_{yz}	$[\bar{1}11]$ $[\bar{1}\bar{1}\bar{1}]$	$[01\bar{1}]$	$[0\bar{1}\bar{1}]$	0	$[0\bar{1}\bar{1}]$	$[011]$
$\vec{E}$ poled	$[\bar{1}1\bar{1}]$ $[\bar{1}\bar{1}1]$	$[011]$	$[01\bar{1}]$	0	$[0\bar{1}1]$	$[01\bar{1}]$

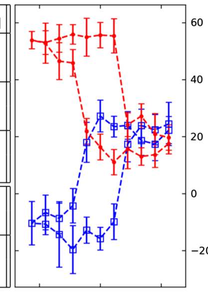

(b) Sample II

Operation	$\mathbf{z}'$	$\mathbf{x}'$	$\mathbf{y}'$	$\mathbf{\Omega}_{[100]}$	$\mathbf{\Omega}_{[010]}$	$\mathbf{\Omega}_{[001]}$
Identity	$[112]$ $[1\bar{1}2]$	$[1\bar{1}0]$ $[110]$	$[11\bar{1}]$ $[\bar{1}11]$	$[11\bar{1}]$ $[\bar{1}11]$	$[\bar{1}\bar{1}1]$ $[\bar{1}11]$	0 0
m_{xz}	$[1\bar{1}2]$ $[112]$	$[110]$ $[1\bar{1}0]$	$[\bar{1}11]$ $[11\bar{1}]$	$[\bar{1}11]$ $[11\bar{1}]$	$[\bar{1}11]$ $[\bar{1}\bar{1}1]$	0 0
m_{xy}	$[11\bar{2}]$ $[1\bar{1}\bar{2}]$	$[1\bar{1}0]$ $[110]$	$[1\bar{1}\bar{1}]$ $[\bar{1}\bar{1}1]$	$[1\bar{1}\bar{1}]$ $[\bar{1}\bar{1}1]$	$[\bar{1}11]$ $[\bar{1}11]$	0 0
m_{yz}	$[\bar{1}12]$ $[\bar{1}\bar{1}2]$	$[\bar{1}\bar{1}0]$ $[\bar{1}10]$	$[1\bar{1}1]$ $[\bar{1}\bar{1}\bar{1}]$	$[\bar{1}1\bar{1}]$ $[111]$	$[\bar{1}1\bar{1}]$ $[\bar{1}\bar{1}\bar{1}]$	0 0
$\vec{E}$ poled	$[\bar{1}1\bar{2}]$ $[\bar{1}\bar{1}\bar{2}]$	$[\bar{1}\bar{1}0]$ $[\bar{1}10]$	$[\bar{1}11]$ $[11\bar{1}]$	$[1\bar{1}\bar{1}]$ $[\bar{1}\bar{1}1]$	$[1\bar{1}\bar{1}]$ $[11\bar{1}]$	0 0

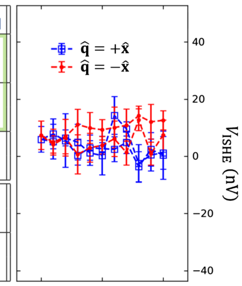

(c) Sample III

Operation	$\mathbf{z}'$	$\mathbf{x}'$	$\mathbf{y}'$	$\mathbf{\Omega}_{[100]}$	$\mathbf{\Omega}_{[010]}$	$\mathbf{\Omega}_{[001]}$
Identity	$[112]$	$[1\bar{1}0]$	$[11\bar{1}]$	$[11\bar{1}]$	$[\bar{1}\bar{1}1]$	0
m_{xz}	$[1\bar{1}2]$	$[110]$	$[\bar{1}11]$	$[\bar{1}11]$	$[\bar{1}11]$	0
m_{xy}	$[11\bar{2}]$	$[1\bar{1}0]$	$[\bar{1}\bar{1}\bar{1}]$	$[\bar{1}\bar{1}\bar{1}]$	$[111]$	0
m_{yz}	$[\bar{1}12]$	$[110]$	$[\bar{1}1\bar{1}]$	$[\bar{1}1\bar{1}]$	$[\bar{1}1\bar{1}]$	0
$\vec{E}$ poled	$[\bar{1}12]$	$[110]$	$[\bar{1}1\bar{1}]$	$[\bar{1}1\bar{1}]$	$[\bar{1}1\bar{1}]$	0

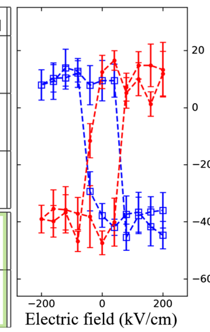

FIG. 3. Calculation of $\mathbf{\Omega_b}$. The polarization directions $\mathbf{z}'$ and cycloid propagation directions $\mathbf{x}'$, as well as the effects of $\vec{E}$ poling, are taken from prior piezoforce microscopy (PFM) and NV work [18,23] on these samples, and Eq. (4) is used to calculate $\mathbf{\Omega_b}$ for the three different samples. The V_{ISHE} hysteresis as a function of poling field for each sample is shown to the right for $\hat{\mathbf{q}} = \pm\hat{\mathbf{x}}$. All data (a)–(c) is consistent with time reversal invariance, and sample II (b) (III (c)) shows m_{xz} (m_{yz}) invariance in all three $\mathbf{\Omega_b}$ (and therefore invariance in $\mathbf{\Omega_b}$ for any $\mathbf{b}$, see Supplemental Material note 6 [24]), as highlighted by the green boxes, and the implications from these invariances are reflected in the data.

Sample II has two types of larger ferroelectric domains, each with their own spin cycloid as given by the $\mathbf{z}'$, $\mathbf{x}'$, and $\mathbf{y}'$ in Fig. 3(b) [17]. The m_{xz} operation effectively maps the cycloids, quantified by $\mathbf{\Omega_b}$, in each domain onto each other, leaving the global magnetic structure invariant up to a domain exchange. Since the population of both domains is the same, a domain exchange leaves the magnon signal invariant, so the sample is effectively invariant under m_{xz}. The implication, as given by Fig. 2, is that $V^{\hat{\mathbf{e}}}(\hat{\mathbf{q}}) = -V^{\hat{\mathbf{e}}}(\hat{\mathbf{q}}) = 0$, and aside from the offset from the $\mathbf{z}$ gradient, the signal is uniformly zero as expected, despite a robust ferroelectric hysteresis (Supplemental Material note 2 [24]). This is an important result: the phenomenological model can be used to predict a lack of V_{ISHE} switching based on the symmetry of the magnetic texture, even without a microscopic understanding of the physics of magnon-spin transport.

Sample III has a single ferroelectric domain with one variant of spin cycloid [17]. Notably for this sample, the effect of the m_{yz} operation on $\mathbf{\Omega_b}$ is identical to the effect of opposite field poling; $m_{yz}(\Psi^{\hat{\mathbf{e}}}) = \Psi^{-\hat{\mathbf{e}}}$. The implications (Fig. 2) are indeed reflected in the data. The main difference between sample II and III is in the global magnetic texture, and our model identifies that the reduced symmetry of the magnetic texture in sample III allows for nonzero V_{ISHE}.

We note that in comparing predictions to experimental data, the model is limited by (a) the ability of the spin-current absorbing contacts to average over the periodicity of the texture (as previously discussed) and (b) any magnetic anomalies created by symmetry-breaking defects. Such defects will add signals that do not obey the implications of the symmetries broken. Despite this, the model still guides the overall understanding and predictions of the physical origin of magnon spin transport in these complicated magnetic textures. For example, we apply these same ideas to predict the detection of magnons created by the spin-Hall effect in the source wire (Supplemental Material note 7 [24]).

In conclusion, we have developed a phenomenological model for magnon-mediated spin transport in multiferroics, which summarizes the dynamics of a magnon mode μ with a phenomenological function η_μ of the experimental configuration. We have shown how this simple model, paired with an analysis of the magnetic texture based on symmetry operations, helps us to explain the behavior of magnon-mediated spin currents. We find that the model's predictions match well with the experimental data for second harmonic nonlocal magnon transport in BFO/Pt based systems. The approach can be extended generally to electric-field-controlled magnon propagation in all multiferroics, and will serve as an important tool for understanding spin currents in future magnon transport studies.

Acknowledgments—This work was primarily supported by the U.S. Department of Energy, Office of Science, Office of Basic Energy Sciences, Materials Sciences and Engineering Division under Contract No. DE-AC02-05CH11231 within the Quantum Materials Program (No. KC2202) and U.S. Department of Energy, Office of Science, Office of Basic Energy Sciences, Materials Sciences and Engineering Division under Contract No. DE-AC02-05-CH11231 [Codesign of Ultra-Low-Voltage Beyond CMOS Microelectronics] for the development of materials for low-power microelectronics. L. W. M. and R. R. also acknowledge the National Science Foundation under Grant No. DMR-2329111 and that this research was partially sponsored by the Army Research Laboratory and was accomplished under Cooperative Agreement No. W911NF-24-2-0100. The views and conclusions contained in this document are those of the authors and should not be interpreted as representing the official policies, either expressed or implied, of the Army Research Laboratory or the U.S. Government. The U.S. Government is authorized to reproduce and distribute reprints for Government purposes notwithstanding any copyright notation herein. Second harmonic generation experiments performed at the Molecular Foundry were supported by the Office of Science, Office of Basic Energy Sciences, of the U.S. Department of Energy under Contract No. DE-AC02-05CH11231. S. K. K. was supported by the Brain Pool Plus Program through the National Research Foundation of Korea funded by the Ministry of Science and ICT (2020H1D3A2A03099291), National Research Foundation of Korea (NRF) grant funded by the Korea government (MSIT) (2021R1C1C1006273), and National Research Foundation of Korea funded by the Korea Government via the SRC Center for Quantum Coherence in Condensed Matter (RS-2023-00207732). J. Í. G. is supported by the Luxembourg National Research Fund (FNR) through Grant No. C21/MS/15799044/FERRODYNAMICS. M. R. and D. G. S. acknowledge the Army Research Office under the ETHOS MURI via cooperative agreement W911NF-21-2-0162. L. C. acknowledges support from the National Science Foundation under Grant No. OIA-2327352.

[1] A. V. Chumak, A. A. Serga, and B. Hillebrands, J. Phys. D **50**, 244001 (2017).
[2] A. Khitun, M. Bao, and K. L. Wang, J. Phys. D **43**, 264005 (2010).
[3] V. V. Kruglyak, S. O. Demokritov, and D. Grundler, J. Phys. D **43**, 264001 (2010).
[4] P. Pirro, V. I. Vasyuchka, A. A. Serga, and B. Hillebrands, Nat. Rev. Mater. **6**, 1114 (2021).
[5] T. Jungwirth, X. Marti, P. Wadley, and J. Wunderlich, Nat. Nanotechnol. **11**, 231 (2016).
[6] J. Han, R. Cheng, L. Liu, H. Ohno, and S. Fukami, Nat. Mater. **22**, 684 (2023).
[7] T. Jungwirth, J. Sinova, A. Manchon, X. Marti, J. Wunderlich, and C. Felser, Nat. Phys. **14**, 200 (2018).
[8] M. Bibes and A. Barthélémy, Nat. Mater. **7**, 425 (2008).
[9] A. Haykal, J. Fischer, W. Akhtar, J.-Y. Chauleau, D. Sando, A. Finco, F. Godel, Y. Birkhölzer, C. Carrétéro, N. Jaouen *et al.*, Nat. Commun. **11**, 1704 (2020).
[10] J. T. Heron, J. L. Bosse, Q. He, Y. Gao, M. Trassin, L. Ye, J. D. Clarkson, C. Wang, J. Liu, S. Salahuddin, D. C. Ralph, D. G. Schlom, J. Íñiguez, B. D. Huey, and R. Ramesh, Nature (London) **516**, 370 (2014).
[11] N. A. Spaldin and R. Ramesh, Nat. Mater. **18**, 203 (2019).
[12] P. Rovillain, R. de Sousa, Y. Gallais, A. Sacuto, M. A. Méasson, D. Colson, A. Forget, M. Bibes, A. Barthélémy, and M. Cazayous, Nat. Mater. **9**, 975 (2010).

[13] S. Manipatruni, D. E. Nikonov, C.-C. Lin, T. A. Gosavi, H. Liu, B. Prasad, Y.-L. Huang, E. Bonturium, R. Ramesh, and I. A. Young, Nature (London) **565**, 35 (2019).

[14] E. Parsonnet, L. Caretta, V. Nagarajan, H. Zhang, H. Taghinejad, P. Behera, X. Huang, P. Kavle, A. Fernandez, D. Nikonov, H. Li, I. Young, J. Analytis, and R. Ramesh, Phys. Rev. Lett. **129**, 087601 (2022).

[15] X. Huang, X. Chen, Y. Li, J. Mangeri, H. Zhang, M. Ramesh, H. Taghinejad, P. Meisenheimer, L. Caretta, S. Susarla *et al.*, Nat. Mater. **23**, 898 (2024).

[16] W. Chen and M. Sigrist, Phys. Rev. Lett. **114**, 157203 (2015).

[17] S. Husain, I. Harris, P. Meisenheimer, S. Mantri, X. Li, M. Ramesh, P. Behera, H. Taghinejad, J. Kim, P. Kavle *et al.*, Nat. Commun. **15**, 5966 (2024).

[18] P. Meisenheimer, M. Ramesh, S. Husain, I. Harris, H. W. Park, S. Zhou, H. Taghinejad, H. Zhang, L. W. Martin, J. Analytis *et al.*, Adv. Mater. **36**, 2404639 (2024).

[19] J. Xiao, G. E. W. Bauer, K. C. Uchida, E. Saitoh, and S. Maekawa, Phys. Rev. B **81**, 214418 (2010).

[20] S. M. Rezende, A. Azevedo, and R. L. Rodríguez-Suárez, J. Phys. D **51**, 174004 (2018).

[21] L. J. Cornelissen, J. Liu, R. A. Duine, J. Ben Youssef, and B. J. van Wees, Nat. Phys. **11**, 1022 (2015).

[22] I. Gross, W. Akhtar, V. Garcia, L. Martínez, S. Chouaieb, K. Garcia, C. Carrétéro, A. Barthélémy, P. Appel, P. Maletinsky *et al.*, Nature (London) **549**, 252 (2017).

[23] P. Meisenheimer, G. Moore, S. Zhou, H. Zhang, X. Huang, S. Husain, X. Chen, L. W. Martin, K. A. Persson, S. Griffin *et al.*, Nat. Commun. **15**, 2903 (2024).

[24] See Supplemental Material at http://link.aps.org/supplemental/10.1103/PhysRevLett.134.016703, which include Refs. [25–28], for additional information about the thin film deposition and device fabrication, magnetic and polarization hysteresis, magnon theory, determination of magnetic texture from microscopy, action of T on the spin cycloid, identity for Ω_b, and extension of model to magnon injection via spin-Hall effect.

[25] D. Rahmedov, D. Wang, J. Íniguez, and L. Bellaiche, Phys. Rev. Lett. **109**, 037207 (2012).

[26] Y.-L. Huang, D. Nikonov, C. Addiego, R. V. Chopdekar, B. Prasad, L. Zhang, J. Chatterjee, H.-J. Liu, A. Farhan, Y.-H. Chu *et al.*, Nat. Commun. **11**, 2836 (2020).

[27] S. R. Burns, O. Paull, J. Juraszek, V. Nagarajan, and D. Sando, Adv. Mater. **32**, 2003711 (2020).

[28] M. Ramazanoglu, M. Laver, I. W Ratcliff, S. M. Watson, W. C. Chen, A. Jackson, K. Kothapalli, S. Lee, S.-W. Cheong, and V. Kiryukhin, Phys. Rev. Lett. **107**, 207206 (2011).

[29] A. Ross, R. Lebrun, M. Evers, A. Deák, L. Szunyogh, U. Nowak, and M. Kläui, Phys. Rev. B **103**, 224433 (2021).

[30] S. Das, A. Ross, X. Ma, S. Becker, C. Schmitt, F. van Duijn, E. F. Galindez-Ruales, F. Fuhrmann, M.-A. Syskaki, U. Ebels *et al.*, Nat. Commun. **13**, 6140 (2022).

[31] H. Adachi, K.-i. Uchida, E. Saitoh, and S. Maekawa, Rep. Prog. Phys. **76**, 036501 (2013).

[32] S. M. Rezende, A. Azevedo, and R. L. Rodríguez-Suárez, J. Appl. Phys. **126**, 151101 (2019).

[33] Here we assume that the spin carried by the magnon is independent of the wave vector k of the magnon, which is not always the case: N. Okuma, Phys. Rev. Lett. **119**, 107205 (2017).

[34] R. S. Fishman, J. T. Haraldsen, N. Furukawa, and S. Miyahara, Phys. Rev. B **87**, 134416 (2013).

[35] J. Shan, L. J. Cornelissen, J. Liu, J. B. Youssef, L. Liang, and B. J. van Wees, Phys. Rev. B **96**, 184427 (2017).

Supplemental Information
Symmetry-based phenomenological model for magnon transport in a multiferroic

Isaac A. Harris,[1,*] Sajid Husain,[2,3,*] Peter Meisenheimer,[3] Maya Ramesh,[4] Hyeon Woo Park,[5] Lucas Caretta,[6] Darrell Schlom,[4] Zhi Yao,[7] Lane W. Martin,[3,8] Jorge Iñiguez,[9,10] Se Kwon Kim,[5] and Ramamoorthy Ramesh[1,3,2,11,8]

[1] *Department of Physics, University of California, Berkeley, CA, USA*
[2] *Materials Science Division, Lawrence Berkeley National Laboratory, Berkeley, CA, USA*
[3] *Department of Materials Science and Engineering, University of California, Berkeley, CA, USA*
[4] *Department of Materials Science and Engineering, Cornell University, Ithaca, USA*
[5] *Department of Physics, Korea Advanced Institute of Science and Technology, Daejon, Korea*
[6] *School of Engineering, Brown University, Providence, RI, USA*
[7] *Applied Mathematics and Computational Research Division, Lawrence Berkeley National Laboratory, Berkeley, CA, 94720, USA*
[8] *Department of Materials Science and NanoEngineering, Rice University, Houston, TX, USA*
[9] *Department of Physics, University of Luxembourg, Luxembourg City, Luxembourg*
[10] *Luxembourg Institute of Science and Technology, Luxembourg*
[11] *Department of Physics and Astronomy, Rice University, Houston, TX, USA*

(Dated: November 20, 2024)

[*] Authors contributed equally

CONTENTS

SUPPLEMENTARY NOTE 1

THIN FILM DEPOSITION AND DEVICE FABRICATION

Lanthanum (La) substituted $BiFeO_3$ ($Bi_{0.85}La_{0.15}FeO_3$) thin films were prepared by pulsed laser deposition (PLD) in an on-axis geometry with a target-to-substrate distance of ∼50 mm using a KrF excimer laser (wavelength 248 nm, COMPex-Pro, Coherent) on $DyScO_3$ (110)substrates. Before the deposition, the substrates were cleaned with IPA and Acetone for 5 min each. The substrates were attached to a heater using silver paint for good thermal contact. $Bi_{0.85}La_{0.15}FeO_3$ layers were deposited with a laser fluence of 1.8 Jcm^{-2} under a dynamic oxygen pressure of 140 mTorr at 710 °C with a 15 Hz laser pulse repetition rate. The samples were cooled down to room temperature at 30 °C/min at a static O_2 atmospheric pressure. The thicknesses were calibrated using X-ray reflectivity.

50 nm thick BFO samples were deposited on TSO substrates using molecular-beam epitaxy

(MBE). MBE films were grown by reactive MBE in a VEECO GEN10 system using a mixture of 80 % ozone (distilled) and 20 % oxygen. Elemental sources of bismuth and iron were used at fluxes of 1.5×10^{14} and $2 \times 10^{13}\,\mathrm{atoms/cm^2s}$ respectively. All films were grown at a substrate temperature of $675\,^{\circ}\mathrm{C}$ and chamber pressure of 5 x 10^{-6} Torr. The thickness was calibrated using X-ray reflectivity.

The prepared samples were immediately transferred to a high vacuum DC magnetron sputtering chamber for Pt deposition. 15 nm of Pt was sputtered at 15W power at room temperature in a 7 mTorr dynamic Ar atmosphere. The thickness was calibrated using atomic force microscopy.

For device fabrication, a positive photoresist (MIR 701), approximately 500 nm thick, was uniformly coated. Photolithography was executed through a Karl Suss MA6 Mask Aligner. Following exposure, the resist underwent wet-etching using MEGAPOSIT MF-26A photoresist developer, and the Pt layer was subsequently ion-milled down to the multiferroic film surface (Intlvac Nanoquest, with a Hiden Analytical SIMS), resulting in the formation of rectangular Pt stripes measuring 120 μm $\times$ 1.3 μm. This process was conducted at the Marvell Nanofabrication laboratory at UC Berkeley.

SUPPLEMENTARY NOTE 2

MAGNETIC AND POLARIZATION HYSTERESIS

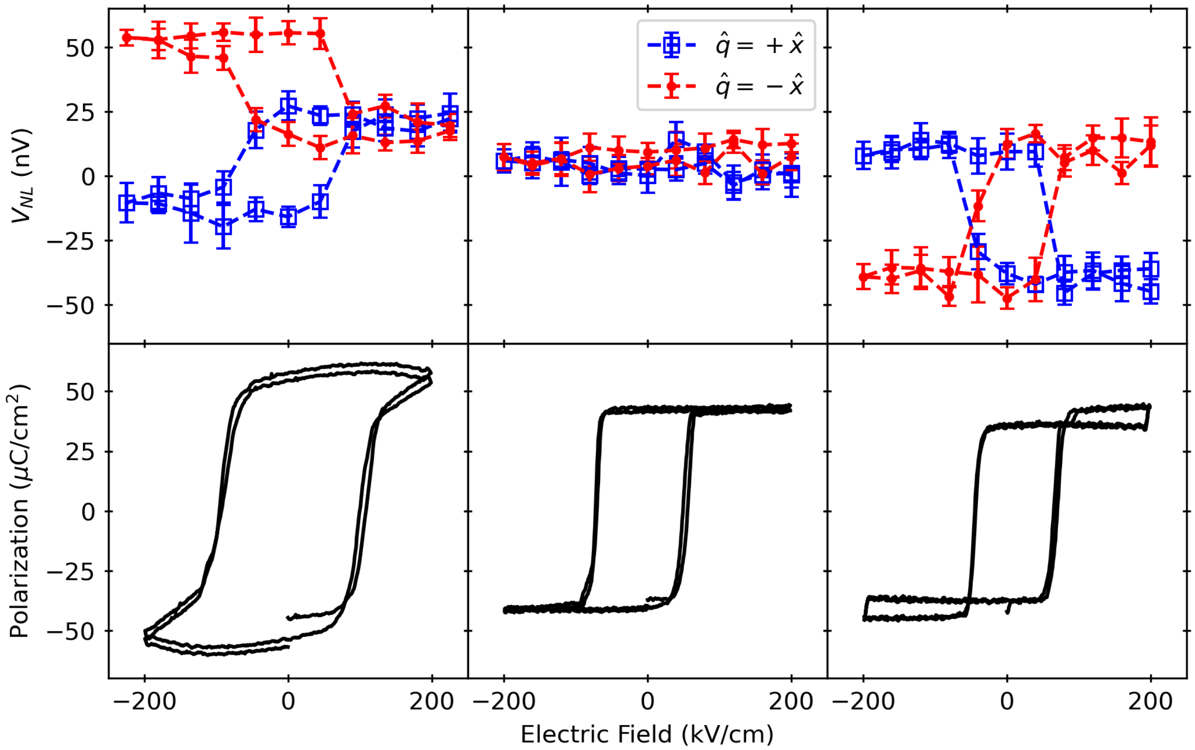

SUPP. FIG. 1. **Nonlocal voltage and Polarization** as a function of electric poling field for the three different samples: 50nm BFO/TSO, two-domain La-doped BFO/DSO, and single-domain La-doped BFO/DSO (left, middle, right). The polarization is a dynamic measurement done with a Radiant Technologies P-PMF. The nonlocal voltage V_{NL} switches when the ferroelectric polarization, and the underlying magnetic state, switches. The nonlocal voltage of the two-domain La-doped BFO/DSO doesn't switch at all because of the symmetries of the magnetic structure.

SUPPLEMENTARY NOTE 3

MAGNON THEORY

In equilibrium, the local magnetization $\mathbf{m}(\mathbf{r})$ will feel an effective field $\mathbf{H}_{\text{eff}} = \delta E/\delta\mathbf{m}(\mathbf{r})$ where E is the magnetic Hamiltonian of the system. Excitations of the local magnetization then follow the dynamics as given by the Landau-Lifshitz-Gilbert (LLG) equation,

$$\dot{\mathbf{m}}(\mathbf{r}) = -\gamma\mathbf{m}\times\mathbf{H}_{\text{eff}}(\mathbf{r}) - \alpha\mathbf{m}\times\dot{\mathbf{m}}, \tag{1}$$

where γ is the gyromagnetic ratio and α is the Gilbert damping. The solutions $\mathbf{m}(\mathbf{r},t)$ of this equation are the magnon modes, labeled by μ and k, where k is the wavevector of the magnon. Since the excitations are bosons, there will be an equilibrium number of magnons in each mode $n^0_{\mu k}(\mathbf{r})$ as given by the Bose-Einstein distribution:

$$n^0_{\mu k}(\mathbf{r}) = \frac{1}{e^{\varepsilon_{\mu k}/k_B T} - 1} \tag{2}$$

Where $\epsilon_{\mu k}$ is the energy of magnon mode μ with wavevector k, k_B is the Boltzmann constant, and T is the temperature. T is a function of position $\mathbf{r}$ (in the case of spin Seebeck), similarly $\epsilon_{\mu k}$ may vary as a function of position if there are different magnetic domains in the sample. In equilibrium, there is no net flow of spin from the multiferroic to an adjacent detector wire, however, the magnons $n_{\mu k}(\mathbf{r})$ in non-equilibrium $n_{\mu k} \neq n^0_{\mu k}$ underneath the detector wire generate a transfer of spin angular momentum and thus a voltage in the electrode via the ISHE. The spin current is given by the spin pumping from the total motion of the magnetization [1, 2], or equivalently from the individual spins of each magnon [2–4]:

$$\mathbf{j}_s(\mathbf{r}) = \tfrac{\hbar}{4\pi} g^{\uparrow\downarrow}\langle \mathbf{m}(t)\times\dot{\mathbf{m}}(t)\rangle \sim \sum_{\mu}\langle\mathbf{S}\rangle_\mu \int d^3k\ v_{\mu k,z}\left(n_{\mu k}-n^0_{\mu k}\right) \tag{3}$$

where $g^{\uparrow\downarrow}$ is the spin mixing conductance, $v_{\mu k,z}$ is the $\mathbf{z}$-component of the magnon group velocity, and $\langle\mathbf{S}\rangle_\mu$ is the spin of magnon mode μ. The time average shows that a linearly oscillating magnetization transfers no spin, but a precessing magnetization does. The summand in Eq. 3 is a generalization of similar equations in thermal magnon studies [2–4] to include any possible modes carrying different spins.

In equilibrium, there is not an excess of magnons beneath the detector wire, however, under a thermal gradient, the diffusion of magnons is governed by the Boltzmann transport equation [3]:

$$n_{\mu k}-n^0_{\mu k} = -\tau_{\mu k}\mathbf{v}_{\mu k}\cdot\nabla_{\mathbf{r}} n^0_{\mu k} - \tau_{\mu k}\mathbf{v}_{\mu k}\cdot\nabla_{\mathbf{r}}\left[n_{\mu k}-n^0_{\mu k}\right], \tag{4}$$

where $\tau_{\mu k}$ is the lifetime of a magnon mode given by scattering rates, including magnon-phonon scattering, and $\mathbf{v}_{\mu\mathbf{k}} = \hat{\mathbf{k}}\frac{\partial\omega_k}{\partial k}$ is the group velocity. Each term and boundary condition is derived from either the temperature gradient, the experimental geometry, or the energetics of magnon modes as given by the magnetic Hamiltonian and ground state of the multiferroic. Due to this excess of magnons, a total spin current can be calculated by integrating the spin current coming from the detector interface:

$$\mathbf{I}_s = \int d^2r\mathbf{j}_s(\mathbf{r}) \sim \sum_{\mu}\langle\mathbf{S}\rangle_\mu \eta_\mu \tag{5}$$

where

$$\eta_\mu = \int d^2r d^3k\ v_{\mu k,z}\left(n_{\mu k}-n^0_{\mu k}\right). \tag{6}$$

Here we have introduced η_μ as the extent to which magnon mode μ contributes its spin $\langle \mathbf{S} \rangle_\mu$ to the detector wire. As a phenomenological function, η_μ is dependent on a) the underlying magnetic Hamiltonian and the magnetic ground state, b) the direction of magnon drift $\hat{\mathbf{q}}$, and c) the device geometry, which is effectively constant throughout all of our studies.

SUPPLEMENTARY NOTE 4

DETERMINATION OF MAGNETIC TEXTURE FROM MICROSCOPY

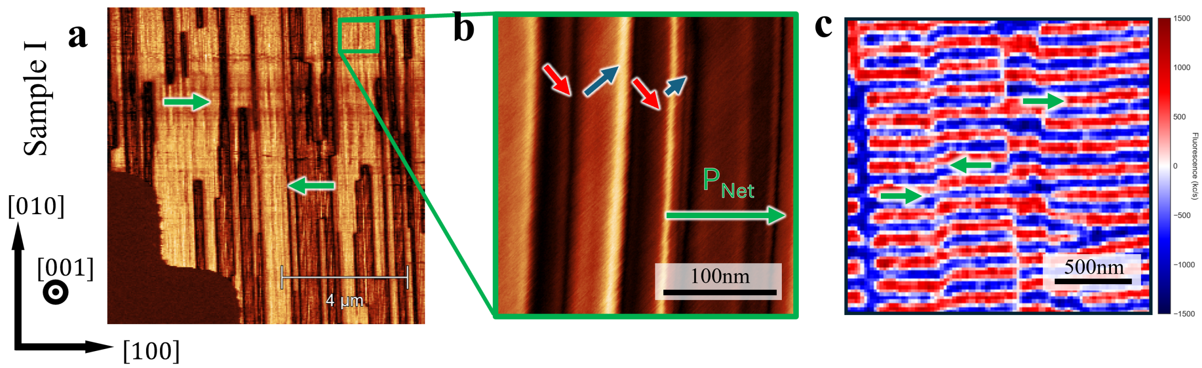

SUPP. FIG. 2. **Ferroelectric and magnetic ground state of Sample I** measured by **a,b** piezoelectric force microscopy (PFM) and **c** nitrogen-vacancy (NV) microscopy. The PFM in **a** shows characteristic large superdomains with net polarization given by the green arrows, and the fine resolution PFM in **b** shows the fine domain structure within the superdomains. The angle between polarization vectors in the fine domains is 109°. In the superdomain with net polarization along [100] ([$\bar{1}$00]), the ferroelectric polarization points along [111] or [1$\bar{1}\bar{1}$] ([$\bar{1}$1$\bar{1}$ or [$\bar{1}\bar{1}$1]), giving rise to a spin cycloid propagation direction along [01$\bar{1}$] ([011]) [5, 6]. The boundary between these two spin cycloids appears in the NV-magnetometry as an antiphase boundary due to the opposite net polarization in two superdomains .

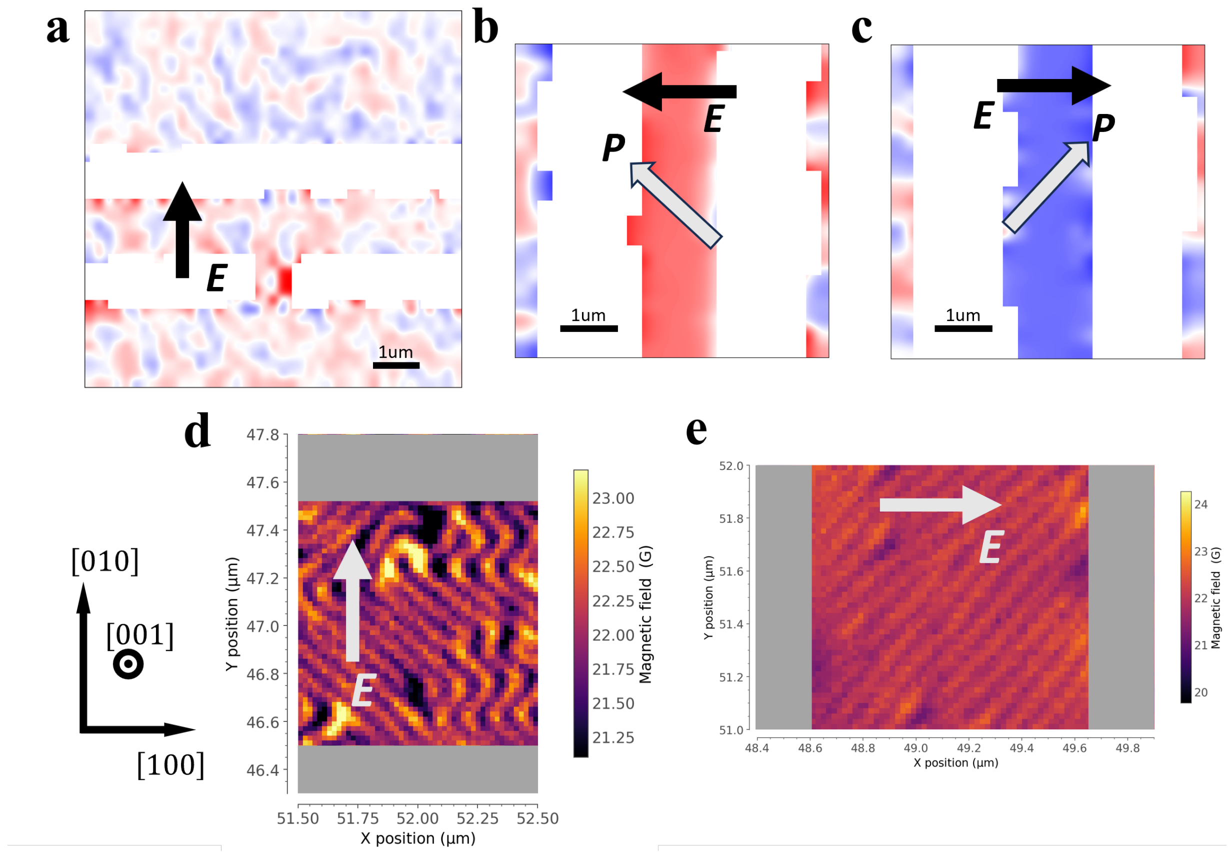

SUPP. FIG. 3. **Ferroelectric and magnetic ground state of Sample II and III** measured by **a-c** Second Harmonic Generation (SHG) and **d-e** NV microscopy. The SHG map shows blue (red) when the in-plane component of polarization is along the [110] ($[\bar{1}10]$) axis. After poling via electric field, we can determine the exact in-plane direction of the polarization. No contrast in the out-of-plane PFM was observed [7]. From prior LBFO studies [7, 8] we know that the polarization is rotated out of plane from the [111] to the [112] directions. The spin cycloid propagation is perpendicular to the polarization, and in the plane, along the axis [110] or $[\bar{1}10]$ depending on the polarization. In sample II (**a,d**), both domains exist even when an electric field is applied, and the spin cycloid in each [112] ($[\bar{1}12]$) domain has a propagation axis along $[\bar{1}10]$ ([110]). In sample III, a single domain forms upon electric field poling, and similarly, a single cycloid domain exists.

SUPPLEMENTARY NOTE 5

ACTION OF $\mathcal{T}$ ON THE SPIN CYCLOID

We consider the case of BFO. The magnetic Hamiltonian given by Fishman *et al.* [9] describes the energy of any given configuration of spins $\mathbf{S}_i$:

$$\begin{aligned} E = &- J_1 \sum_{\langle i,j \rangle} \mathbf{S}_i \cdot \mathbf{S}_j - J_2 \sum_{\langle i,j \rangle'} \mathbf{S}_i \cdot \mathbf{S}_j - K \sum_i S_{iz'}^2 \\ &- D_1 \sum_{\mathbf{R}_j = \mathbf{R}_i + a'\mathbf{x}'} \mathbf{y}' \cdot (\mathbf{S}_i \times \mathbf{S}_j) \\ &- D_2 \sum_{\mathbf{R}_j = \mathbf{R}_i + a\mathbf{x}, a\mathbf{y}, a\mathbf{z}} (-1)^{R_{iz'}/c} \mathbf{z}' \cdot (\mathbf{S}_i \times \mathbf{S}_j) \, . \end{aligned} \tag{7}$$

Here, the exchange constants J_1 and J_2 and the pairs of spins $\langle i, j \rangle$ and $\langle i, j \rangle'$ are for nearest neighbor spins and second nearest neighbor spins respectively. K is the anisotropy constant. The primed basis vectors $\mathbf{x}'$, $\mathbf{y}'$, and $\mathbf{z}'$ are rotated from the unprimed basis vectors so that $\mathbf{z}'$ lies along the direction of the polarization, $\mathbf{x}'$ lies along the propagation vector of the spin cycloid, and $\mathbf{y}' = \mathbf{z}' \times \mathbf{x}'$, as shown in Fig. 1c (main text). The ground state of the magnetic Hamiltonian is the spin cycloid and spin-density wave with a period $\sim$70nm and no net magnetization [9–12], and is also given by Fishman et al [9]:

$$S_{x'}(\mathbf{R}) = (-1)^{R_{z'}/c} \cos\tau \sqrt{S^2 - S_{z'}(\mathbf{R})^2} \times \mathrm{sgn}[\sin(kR_{x'})] \tag{8}$$

$$S_{y'}(\mathbf{R}) = \sin\tau \sqrt{S^2 - S_{z'}(\mathbf{R})^2} \times \mathrm{sgn}[\sin(kR_{x'})] \tag{9}$$

$$S_{z'}(\mathbf{R}) = (-1)^{R'_z/c} S \sum_{n=1,3...}^{\infty} C_n \cos(nkR_{x'}), \tag{10}$$

where the odd-order coefficients C_n satisfy $\sum_{n=1,3...}^{\infty} C_n = 1$ and give the anharmonicity of the cycloid, τ is a variational parameter, and $k\hat{\mathbf{x}}'$ is the spin cycloid propagation vector.

The action of time reversal $\mathcal{T}$ on the spins $\mathbf{S}(\mathbf{R})$ is to negate each spin:

$$\mathcal{T}\left[\mathbf{S}(\mathbf{R})\right] = -\mathbf{S}(\mathbf{R}) \tag{11}$$

Consider the action of a translation by $\hat{\mathbf{x}}'\pi/k$. We show that $\mathbf{S}(\mathbf{R}') = -\mathbf{S}(\mathbf{R})$ where $\mathbf{R}' = \mathbf{R} + \hat{\mathbf{x}}'\pi/k$.

$$S_{x'}(\mathbf{R}') = (-1)^{R_{z'}/c} \cos\tau \sqrt{S^2 - S_{z'}(\mathbf{R}')^2} \times \mathrm{sgn}[\sin(kR_{x'} + \pi)] = -S_{x'}(\mathbf{R}) \tag{12}$$

$$S_{y'}(\mathbf{R}') = \sin\tau \sqrt{S^2 - S_{z'}(\mathbf{R}')^2} \times \mathrm{sgn}[\sin(kR_{x'} + \pi)] = -S_{y'}(\mathbf{R}) \tag{13}$$

$$S_{z'}(\mathbf{R}') = (-1)^{R'_z/c} S \sum_{n=1,3\ldots}^{\infty} C_n \cos(nkR_{x'} + n\pi) = -S_{z'}(\mathbf{R}) \tag{14}$$

Therefore the action of time reversal $\mathcal{T}$ is equivalent to a translation and the magnon dynamics are effectively invariant under $\mathcal{T}$.

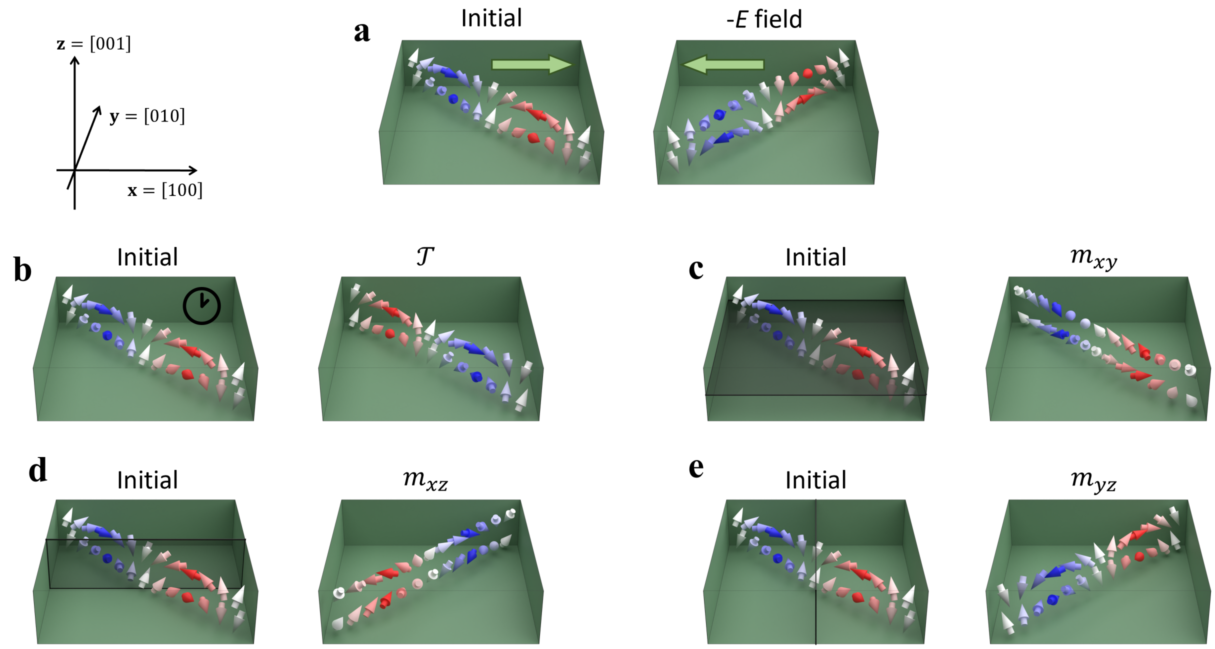

SUPP. FIG. 4. **Symmetry operations, as discussed in the main text Figure 2, acting on a spin cycloid.** (a) The cycloid symmetry is poled initially to the right ($+\hat{\mathbf{x}}$ direction), and then poled with the opposite field, where the polarization undergoes a 71° rotation. The action of (b) time reversal ($\mathcal{T}$) and the (c) m_{xy}, (d) m_{xz}, and (e) m_{yz} mirror operations on the initial spin cycloid is shown. We note that the arrows represent an average local magnetic moment, with spin-density-wave canting and spin cycloid rotation exaggerated for the viewer's sake. The red shading denotes a local net moment in $+\hat{\mathbf{z}}$, while the blue shading denotes a local net moment in $-\hat{\mathbf{z}}$. Under mirror operations, position transforms as a vector and spin transforms as a pseudovector.

SUPPLEMENTARY NOTE 6

IDENTITY FOR $\mathbf{\Omega_b}$

Here we show that if $\mathbf{\Omega_b}$ is invariant under some operation $\mathcal{O}$ for 3 independent $\mathbf{b}$, then $\mathbf{\Omega_b}$ is invariant for any vector $\mathbf{b}$. Suppose for $i = 1, 2$, $\mathcal{O}[\mathbf{\Omega}_{\mathbf{b}_i}] = \mathbf{\Omega}_{\mathbf{b}_i}$. Recall,

$$\mathbf{\Omega_b} = (\mathbf{b} \cdot \mathbf{x}')\mathbf{y}' \tag{15}$$

For any constant a, it follows that

$$\mathbf{\Omega}_{\mathbf{b}_1 + a\mathbf{b}_2} = ((\mathbf{b}_1 + a\mathbf{b}_2) \cdot \mathbf{x}')\mathbf{y}' = (\mathbf{b}_1 \cdot \mathbf{x}')\mathbf{y}' + a(\mathbf{b}_2 \cdot \mathbf{x}')\mathbf{y}' = \mathbf{\Omega}_{\mathbf{b}_1} + a\mathbf{\Omega}_{\mathbf{b}_2} \tag{16}$$

Since symmetry operations are linear, it follows that

$$\mathcal{O}[\mathbf{\Omega}_{\mathbf{b}_1 + a\mathbf{b}_2}] = \mathcal{O}[\mathbf{\Omega}_{\mathbf{b}_1}] + a\mathcal{O}[\mathbf{\Omega}_{\mathbf{b}_2}] = \mathbf{\Omega}_{\mathbf{b}_1} + a\mathbf{\Omega}_{\mathbf{b}_2} = \mathbf{\Omega}_{\mathbf{b}_1 + a\mathbf{b}_2} \tag{17}$$

Therefore, if $\mathbf{\Omega_b}$ is invariant under $\mathcal{O}$ for vectors $\mathbf{b}_i$, for any linear combination $\mathbf{b}'$ of the $\mathbf{b}_i$, $\mathbf{\Omega}_{\mathbf{b}'}$ is invariant under $\mathcal{O}$. So, to show that $\mathbf{\Omega_b}$ is invariant under $\mathcal{O}$ for any vector $\mathbf{b}$, it suffices to show that $\mathbf{\Omega}_{\mathbf{b}_i}$ is invariant under $\mathcal{O}$ for three independent basis vectors $\mathbf{b}_i$.

SUPPLEMENTARY NOTE 7

EXTENSION OF MODEL TO MAGNON INJECTION VIA SPIN-HALL EFFECT

When a spin current $\mathbf{I}_s^i$ (where the vector component denotes the spin polarization) is injected into the magnetic insulator, magnons in mode μ with spin $\langle \mathbf{S} \rangle_\mu$ are created with proportionality to $\mathbf{I}_s^i \cdot \langle \mathbf{S} \rangle_\mu$, and absorbed if the dot product is negative. This creates a concentration gradient in the magnon population across the device, and the resulting diffusion of magnons leads to a spin accumulation at the interface of the detector wire and the magnetic insulator. Let the wires be along $\hat{\mathbf{y}}$ and the film normal along $\hat{\mathbf{z}}$, so magnons diffuse along $\pm\hat{\mathbf{x}}$. To denote the location of the detector wire with respect to the source wire, we use $\hat{\mathbf{q}}' = \pm\hat{\mathbf{x}}$, identical to $\hat{\mathbf{q}}$ in the V_{SSE} studies. Furthermore, the injected spin current polarization is $\mathbf{I}_s^i = I_s^i \hat{\mathbf{x}}$. The resulting spin current into the detector wire $\mathbf{I}_s^d$ then has the form

$$\mathbf{I}_s^d \sim \sum_\mu I_s^i \, \langle S_x \rangle_\mu \, \langle \mathbf{S} \rangle_\mu \, \eta_\mu^{\hat{\mathbf{e}}} \left(\mathrm{sgn}[I_s^i \langle S_x \rangle_\mu] \hat{\mathbf{x}} \right). \tag{18}$$

Here we have the state of the multiferroic represented by $\hat{\mathbf{e}}$. There are two factors of the spin of the magnon $\langle \mathbf{S} \rangle_\mu$ because of the creation and absorption processes that happen at the source and detector. The voltage measured across the detector wire V_{SHE} is then proportional to $\mathbf{I}_s^d \cdot \hat{\mathbf{x}}$, and is measured referencing the first harmonic of a lock-in, which time averages the product of the signal and the alternating source current. In such an alternating current, $I_s^i > 0$ for half the cycle, and $I_s^i < 0$ for the other half of the cycle, so the measured voltage is proportional to

$$V_{SHE} \sim \sum_\mu \langle S_x \rangle_\mu^2 \eta_\mu^{\hat{\mathbf{e}}}(+\hat{\mathbf{x}}) + \sum_\mu \langle S_x \rangle_\mu^2 \eta_\mu^{\hat{\mathbf{e}}}(-\hat{\mathbf{x}}). \tag{19}$$

Another way to think about this is to consider one magnon mode μ_1 with spin $\langle S_x \rangle_{\mu_1} = \hbar$.

Magnons in this mode will be created and diffuse in $+\hat{\mathbf{x}}$ when $I_s^i > 0$, invoking $\eta_{\mu_1}^{\hat{\mathbf{e}}}(+\hat{\mathbf{x}})$. However magnons in this mode will also be annihilated at the source and diffuse in $-\hat{\mathbf{x}}$ when $I_s^i < 0$, invoking $\eta_{\mu_1}^{\hat{\mathbf{e}}}(-\hat{\mathbf{x}})$. So, the signal V_{SHE} is a sum of both of those events.

We now suppose that we can choose the state between $\hat{\mathbf{e}} = \pm\hat{\mathbf{x}}$ by applying an electric field between the source and detector wires, and make a hysteresis measurement to measure $V_{SHE}^{+\hat{\mathbf{x}}} - V_{SHE}^{-\hat{\mathbf{x}}}$. The difference ΔV_{SHE} is then

$$\Delta V_{SHE} \sim \sum_{\mu} \Big[\langle S_x \rangle_\mu^2 \eta_\mu^{+\hat{\mathbf{x}}}(+\hat{\mathbf{x}}) + \langle S_x \rangle_\mu^2 \eta_\mu^{+\hat{\mathbf{x}}}(-\hat{\mathbf{x}}) - \langle S_x \rangle_\mu^2 \eta_\mu^{-\hat{\mathbf{x}}}(+\hat{\mathbf{x}}) - \langle S_x \rangle_\mu^2 \eta_\mu^{-\hat{\mathbf{x}}}(-\hat{\mathbf{x}}) \Big]. \quad (20)$$

Notice, that if we now switch the identity of the source and detector wire, changing $\hat{\mathbf{q}}'$ from $+\hat{\mathbf{x}}$ to $-\hat{\mathbf{x}}$ which effectively sends $\eta_\mu^{\hat{\mathbf{e}}}(\hat{\mathbf{q}}) \rightarrow \eta_\mu^{\hat{\mathbf{e}}}(-\hat{\mathbf{q}})$, the expression remains unchanged and we expect to recover a hysteresis with the same polarity and the same differential. We use $SrIrO_3$ electrodes to measure the first harmonic hysteresis, and our preliminary results reflect the model results (Supp. Fig. 5).

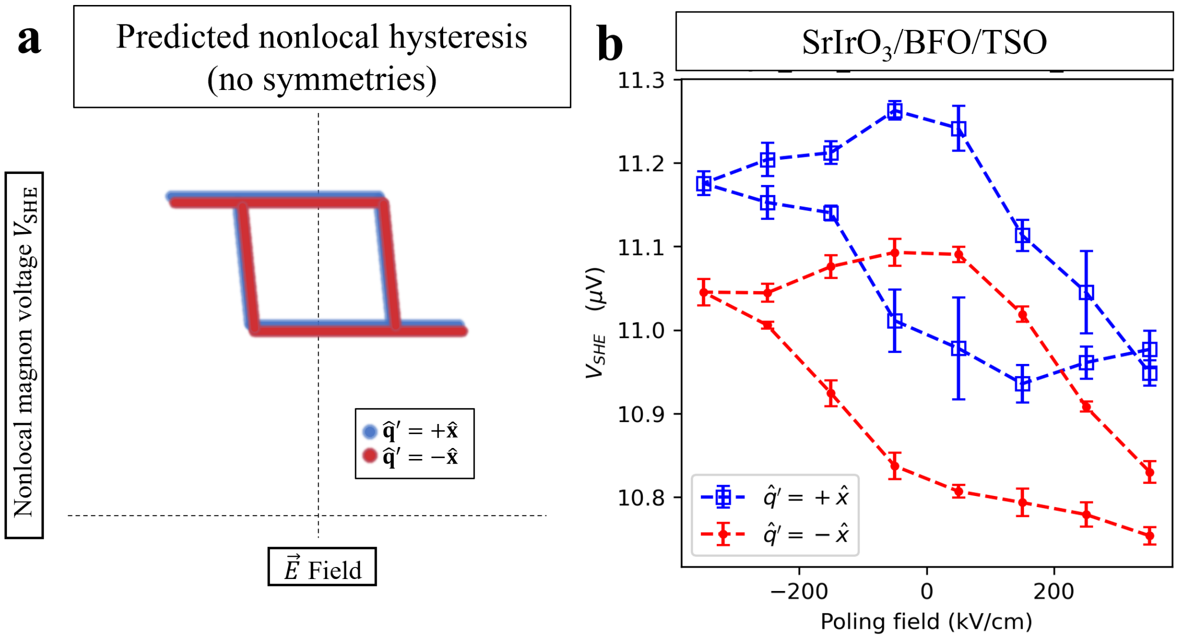

SUPP. FIG. 5. **Spin-Hall effect magnon voltage, predicted and measured** as a function of electric poling field. Predicted hysteresis with no (m_{yz}) symmetry constraints is shown in **a** (**c**). **b** shows V_{SHE} hysteresis measured using $SrIrO_3$ source and detector on BFO with magnetic texture identical to sample I, with no symmetries besides $\mathcal{T}$ invariance. The distorted shape of the hysteresis is likely due to systematic issues in the quality of the $SrIrO_3$ electrodes such as resistive heating. The differing offsets are likely from systematic differences between the circuits for $\hat{\mathbf{q}}' = +\hat{\mathbf{x}}$ and $\hat{\mathbf{q}}' = -\hat{\mathbf{x}}$.

[1] J. Xiao, G. E. W. Bauer, K.-c. Uchida, E. Saitoh, and S. Maekawa, Phys. Rev. B **81**, 214418 (2010).

[2] H. Adachi, K.-i. Uchida, E. Saitoh, and S. Maekawa, Reports on Progress in Physics **76**, 036501 (2013).

[3] S. M. Rezende, A. Azevedo, and R. L. Rodríguez-Suárez, J. Phys. D: Appl. Phys. **51**, 174004 (2018).

[4] S. M. Rezende, A. Azevedo, and R. L. Rodríguez-Suárez, Journal of Applied Physics **126**, 151101 (2019).

[5] P. Meisenheimer, G. Moore, S. Zhou, H. Zhang, X. Huang, S. Husain, X. Chen, L. W. Martin, K. A. Persson, S. Griffin, *et al.*, Nature Communications **15**, 2903 (2024).

[6] P. Meisenheimer, M. Ramesh, S. Husain, I. Harris, H. W. Park, S. Zhou, H. Taghinejad, H. Zhang, L. W. Martin, J. Analytis, *et al.*, Advanced Materials **36**, 2404639 (2024).

[7] S. Husain, I. Harris, P. Meisenheimer, S. Mantri, X. Li, M. Ramesh, P. Behera, H. Taghinejad, J. Kim, P. Kavle, *et al.*, Nature communications **15**, 5966 (2024).

[8] Y.-L. Huang, D. Nikonov, C. Addiego, R. V. Chopdekar, B. Prasad, L. Zhang, J. Chatterjee, H.-J. Liu, A. Farhan, Y.-H. Chu, *et al.*, Nature communications **11**, 2836 (2020).

[9] R. S. Fishman, J. T. Haraldsen, N. Furukawa, and S. Miyahara, Physical Review B **87**, 134416 (2013).

[10] S. R. Burns, O. Paull, J. Juraszek, V. Nagarajan, and D. Sando, Advanced Materials **32**, 2003711 (2020).

[11] M. Ramazanoglu, M. Laver, I. W Ratcliff, S. M. Watson, W. Chen, A. Jackson, K. Kothapalli,

S. Lee, S.-W. Cheong, and V. Kiryukhin, Physical review letters **107**, 207206 (2011).

[12] D. Rahmedov, D. Wang, J. Íniguez, and L. Bellaiche, Physical review letters **109**, 037207 (2012).